Inertia Welding Nickel-Based Superalloy: Part I. Metallurgical Characterization

M. PREUSS, J.W.L. PANG, P.J. WITHERS, and G.J. BAXTER

This article describes a quantitative study of the microstructure of nickel-based superalloy RR1000 tube structures joined by inertia welding. One as-welded and three post weld heat-treated (PWHT) conditions have been investigated. The samples were characterized mechanically by measuring the hardness profiles and microstructurally in terms of γ grain size, γ' precipitate size and volume fraction, stored energy, and microtexture. Electron backscatter diffraction (EBSD) was used to characterize high-angle grain boundaries (HAGB) and the variation of microtexture across the weld line. The coherent γ' precipitates were investigated over a range of scales on etched samples in a field emission gun scanning electron microscope (FEGSEM), using carbon replicas in a transmission electron microscope (TEM) and from thin slices by means of high-energy synchrotron X-rays. Dramatic changes in the microstructure were observed within 2 mm of the weld line. In this region, the hardness profile is influenced by changes in grain size, γ' volume fraction, γ' particle size, and the work stored in the material. Further away, the observed hardness variation is still significant although only minor microstructural changes could be observed. In this region, the correlation of microstructure and hardness is less straightforward. Here, a combination of small microstructural changes appears to give rise to a significant change in strength. No significant texture or grain distortion was observed in the extensively plastically deformed region due to recrystallization.

I. INTRODUCTION

A NEW generation of nickel-based superalloys having a significantly higher volume fraction of γ' then conventional superalloys has been developed to meet the demand for better high-temperature properties. These alloys are usually very difficult to weld and are prone to microcracking as solidification takes place during welding.[1,2] Therefore, inertia welding is a very attractive welding process because it does not involve any melting, provided optimum welding parameters are chosen. Furthermore, it is more suitable for mass production than electron-beam welding.[3]

In inertia welding, an axisymmetric workpiece is rotated to a specific speed and then a second stationary workpiece is forced into frictional engagement with the first. The frictional heat is sufficient to soften the two components in the weld region without introducing melting. In some respects, inertia welding resembles a high-speed forging process in which the upset (the extent to which the workpieces are foreshortened) creates the flash but with only the near-weld zone reaching forging temperatures.

Because of the extreme thermomechanical history, the microstructure is heavily modified in the heat-affected zone (HAZ) of a joint. It is generally believed that, at the weld line, dynamic recrystallization takes place.[4] Furthermore, because of the steep temperature and plastic-deformation gradients in the HAZ, it is possible that near the weld line a work-hardened zone will be present. It is important to characterize the microstructure in this area because it will have a significant impact on the mechanical properties of the assembly. This article focuses on the variations in microstructure as a function of position and heat treatment caused by inertia welding RR1000. A companion article[5] describes the concomitant variation of residual stress in the same welds.

RR1000 is a recently developed powder-processed, high-strength nickel-based superalloy. It is being considered for high-pressure turbine disks in the next generation of gas turbine aeroengines.[6] It comprises a high volume fraction of primary γ' (1 to 3 μm), secondary γ' (50 to 500 nm), and tertiary γ' (5 to 30 nm). In the parent alloy, particles of γ', which remain undissolved during the solution heat-treatment stage (primary γ'), delineate γ-grain boundaries, while intragranular γ' occurs upon cooling in a bimodal distribution (secondary and tertiary γ'). Whereas particles of secondary γ' nucleate at an early stage during quenching from the solution temperature, tertiary γ' nucleates at a lower temperature, when diffusion rates are slow, and secondary γ' cannot grow sufficiently quickly during cooling.[7]

Various studies of inertia welded nickel-based superalloys in the as-friction welded condition have shown two different types of hardness profiles in the HAZ. Alloys, such as Waspaloy, which contain about 25 pct γ' generally exhibit a pronounced hardness drop, which is attributed to the absence of γ' in this region after welding.[8,9] However, alloys, such as N18 and Astroloy, which contain about 50 pct γ', show a hardness peak in the HAZ. This is due to the great driving force of the alloying elements to precipitate even at extremely high cooling rates.[10] The present study aims to build on earlier work by providing a comprehensive picture of the microstructural aspects governing the hardness variation in as-welded and postweld heat-treated (PWHT) welds.

M. PREUSS, Research Fellow, and P.J. WITHERS, Professor, are with the Manchester Materials Science Centre, University of Manchester and UMIST, Manchester M1 7HS, United Kingdom. Contact e-mail: michael.preuss@man.ac.uk J.W.L. PANG, Research Fellow, is with the Oak Ridge National Laboratory, Oak Ridge, TN 37830. G.J. BAXTER, Process Metallurgist, is with Rolls-Royce plc., Derby DE24 8BJ, United Kingdom.

Manuscript submitted November 19, 2001.

Table I. Chemical Composition (Weight Percent, Balance Nickel) of RR1000 and Other Disc Alloys

Alloy	Cr	Co	Mo	W	Al	Ti	Ta	Hf	Zr	C	B
RR1000	14.35 to 15.15	14.0 to 19.0	4.25 to 5.25	—	2.85 to 3.15	3.45 to 4.15	1.35 to 2.15	0.0 to 1.0	0.05 to 0.07	0.012 to 0.033	0.01 to 0.025
U720LI	16	15	3.0	1.25	2.5	5.0	—	—	0.035	0.015	0.015
WASPALOY	19.5	13.5	4.3	—	1.3	3.0	—	—	—	0.08	0.006

Table II. Conditions of the Samples Tested

Condition	Sample Number
As-welded	S1
Conventional PWHT	S2
Modified PWHT (+50 °C)	S3
Modified (2) PWHT (+150 °C)	S4

Table III. Chemical Composition of the γ' Etchant

Part 1	Part 2
150 ml H_2O	15 ml HNO_3
150 ml HCL	25 ml H_2O
2.5 g MoO_3	30 ml part 1

II. EXPERIMENTAL

A. *Materials and Specimens*

The chemical composition of RR1000[6] is listed in Table I alongside those for UDIMET* 720LI and WASPALOY**[11] for comparison. This shows that RR1000 has a much larger weight percent of Al and Ti than WASPALOY and, consequently, a significantly higher volume fraction of γ' (γ' is $(Ni, Co)_3$ (Al, Ti)[12]). This is expected to markedly affect the development of microstructure and residual stress. The RR1000 material used for this investigation came from an isothermal pancake forging, fully heat-treated and annealed. Rings with an outer diameter (OD) of 143 mm, a wall thickness of 11 mm, and an axial length of 50 mm were machined from the pancake and subsequently inertia welded at MTI (South Bend, IN). For the microstructural studies described in this article, four samples, S1 to S4, were machined across the weld line of one welded assembly. Three identically sized samples of the as-welded material were PWHT in a tube furnace using an inert argon atmosphere and subsequently air cooled. Table II summarizes the conditions of the samples tested. The samples were subsequently cut into slices for different investigations.

*UDIMET is a trademark of Special Metals Corporation, New Hartford, NY.

**WASPALOY is a trademark of Precision Rings, Inc., Indianapolis, IN.

B. *Hardness Testing*

To study the microstructure after hardness testing, γ' was dissolved from the polished surfaces using an etchant; the composition of which is given in Table III. Hardness testing was then carried out under a load of 1 kg using a calibrated, Vickers-hardness indentation machine. This was found to be an optimum load, resulting in indentations (60 to 70 μm), considerably larger then the γ grain size (10 μm), but still small enough to avoid averaging the hardness profile over too large a distance in the axial direction. The polished and etched samples were aligned with the indented surface perpendicular to the hoop direction. For each sample, measurements were carried out on a grid of five lines parallel to the axial direction and spaced greater than four indentations apart. Measurements were taken from the weld line to a distance 9 mm away from it, with smaller increments close to the weld line. The accuracy of the axial position of the indentation marks was estimated to be within 20 μm. The results presented are the average of the five measurements per axial position.

C. *Synchrotron X-ray Measurements*

Diffraction-profile measurements can be used to assess the fraction of γ' across the welded region. To this end, high resolution, synchrotron X-ray diffraction-profile measurements were carried out on the ID11 beam line at the European Synchrotron Radiation Facility (Grenoble, France) using a scanned serial detector. Measurements were made in transmission on slices cut from the inertia welded tube so as to contain the axial and radial directions and then electropolished to an average thickness of 0.5 mm. A monochromatic beam of 60 keV energy (λ = 0.208321 Å) was stopped down by slits to 150 μm in the axial and 3 mm in the radial direction and scanned (axially) across the weld. The high intensity of the synchrotron beam allowed accurate measurements of the (100) superlattice reflection, arising from the ordered γ' phase (LI_2 structure). Because the (100) refection was systematically absent for the disordered γ-matrix phase, by normalizing the integrated intensity of the superlattice reflection with the integrated intensity of the (200) reflection, any influence of the texture on the measurement could be eliminated, and the obtained value related to the volume fraction of γ'.[13,14,15] As it was expected that the intensity of the (100) reflection would be weakest at the weld line, the counting time was increased to 45 minutes (from 8 minutes) in this region. In addition to the (100) and (200) reflections, the (111), (220), and (311) reflections were also measured. The counting time for the composite $\gamma + \gamma'$ diffraction peaks was 5 seconds. Measurements were performed on samples S1, S2, and S3 and for the (111) reflection also on S4. In addition to the integrated intensity, the lattice parameter[5] and the full-width half-maximum (FWHM) variations were also mapped.

D. *Electron Microscopy and Image Analysis*

The secondary and tertiary γ' sizes are large enough to be quantified by electron microscopy. The dramatic change in microstructure within a range of millimeters from the

weld line required very careful sample preparation. For imaging γ', one would normally use the dark-field imaging technique or carbon replicas in a transmission electron microscope (TEM). However, in view of the need to determine the axial position of the area studied very accurately (± 50 μm), these techniques are not ideal because they rely on extracting samples for TEM. Therefore, a PHILIPS* XL30 field emission gun scanning electron microscope (FEGSEM) in the secondary electron mode at 8 kV was used to analyze the axial changes in microstructure of each sample at a working distance of 10 mm. The hardness-indentation marks were used as reference markers for axial position in the FEGSEM. The high resolutions of the FEGSEM allowed the analysis of primary, secondary, and, in the case of the modified PWHT samples, the tertiary γ'. The volume fraction of primary γ' was obtained by studying the samples at a low magnification (5 images per axial position) and using the mean linear-intercept method.

*PHILIPS is a trademark of Philips Electronic Instruments Corps. Mahwah, NJ.

The image analysis of secondary and tertiary γ' was carried out using the Kontron KS 400 software package (HKL Technology, Hobro, Denmark). Five images at each axial position were taken within γ grains, avoiding primary γ'. Consequently, the determined volume fractions of secondary and tertiary γ' should be regarded as values in the center of γ grains and not a true overall value. The magnification was chosen such that 100 to 150 secondary γ' particles could be counted. It was only possible to study tertiary γ' for samples S3 and S4, as it was too fine in the as-welded (S1) and conventional PWHT (S2) samples. For these samples, the volume fraction of tertiary γ' was estimated by subtracting the primary and secondary volume fractions determined by image analysis from the total γ' fraction determined from the normalized integrated X-ray intensity of the (100) reflection.

Because of the difficulty of direct observation in the FEGSEM, the tertiary γ' at the weld line was observed by taking carbon replicas. For each sample condition, slices were cut perpendicular to the axial direction (*i.e.*, parallel to the plane of the weld) and subsequently ground and polished down precisely to the weld plane. This location could be determined accurately because of the disappearance of the primary γ' at the weld line, as determined by optical microscopy. Samples were polished to 1 μm using standard metallographical techniques, before being lightly etched electrolytically at 2 to 3 V in aqueous 10 pct phosphoric acid. To clean the samples, a solution of 3 pct nitrocellulose in amyl acetate was placed on the prepared surface. After drying, the film was removed along with any over extracted particles. Carbon coating was applied using a PHILIPS high-vacuum unit. The replicas were detached by etching electrolytically at up to 10 V in 20 pct perchloric acid in ethanol. The carbon replicas were then placed on copper grids and imaged in a PHILIPS EM440T TEM.

E. *Electron Backscatter Diffraction*

Automated electron backscatter diffraction (EBSD) mapping can provide a great deal of information about grain statistics. During EBSD mapping, the beam was scanned over the polished sample, which was tilted 70 deg to the backscatter detector of a PHILIPS XL30 FEGSEM. The EBSD patterns were detected by a charge-coupled device camera with the background subtracted using an image processor. Microscope control, pattern acquisition, and solution were carried out with the HKL Channel system. Seven area maps were acquired across the weld line using a scanning step size between 0.27 and 0.35 μm. The EBSD data were analyzed using VMAP, an in-house software development by Humphreys *et al.*,[16] to obtain the grain size, orientation distribution, misorientation distribution, and stored energy. Reconstruction of the grains from the orientation data was made, and the grain diameters were determined from the "equivalent circle diameter" according to $D_e = (4\ A/\pi)^{1/2}$, where A is the area of the grain. To assess the level of plastic deformation experienced by the material, the stored energy was determined for each map. The VMAP software package enabled a calculation of the mean boundary energy associated with each pixel by calculating its misorientation to the adjacent pixels. From this, a measure of the stored energy was calculated from the Read–Shockley equation used in a form where the energy (γ) and misorientation (θ) are normalized with respect to the values of those parameters (γ_m and θ_m) when the boundary becomes a high-angle boundary (*i.e.*, $\theta \sim 15$ deg):[17]

$$\gamma = \gamma_m \frac{\theta}{\theta_m}\left(1 - \ln \frac{\theta}{\theta_m}\right) \qquad [1]$$

The value of the high-angle grain-boundary (HAGB) energy used for Ni was 0.866 J/m^2 according to Reference 18. The texture calculated from the EBSD maps was analyzed using the Channel software package.[19]

III. RESULTS AND DISCUSSION

A. *Hardness Profiles*

Steep gradients in the hardness are observed for the as-welded condition (Figure 1(a)). A trough in hardness occurring approximately 1 mm from the join line is bounded by two peaks situated at 0.3 and 2 mm from the weld line. The hardness is above that recorded for the parent at all positions. This is to be expected for a high γ' containing alloy, as the large driving force for alloying elements to precipitate even at high cooling rates results in a very effective γ' distribution (high volume fraction of tertiary γ').[8,10] After conventional postweld heat treatment, an increase in hardness in the weld region is observed such that the peak at 2 mm is subsumed within the upward curve towards the weld line, and the trough is replaced by a discontinuity in slope. An increase in hardness of around 50 HV is observed near the weld line.

Figure 1(b) compares the hardness profiles for samples S2, S3, and S4. An increase of 50 °C to the conventional postweld heat treatment temperature does not result in any major changes of the hardness profile or peak-hardness value. However, the discontinuity observed at 1 mm in sample S2 has disappeared. The hardness profile of S4 (+150 °C above the conventional postweld heat treatment) has dropped significantly to lower hardness values. The hardness profile of S4 shows a peak hardness (at 490 HV) that is now closer to the weld line than the peak for S2 and S3. In the following sections, emphasis is placed on analyzing the variation of

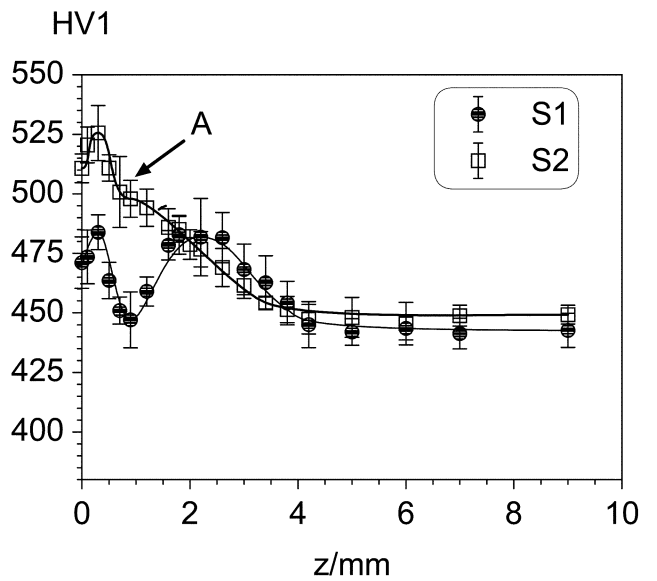

(*a*)

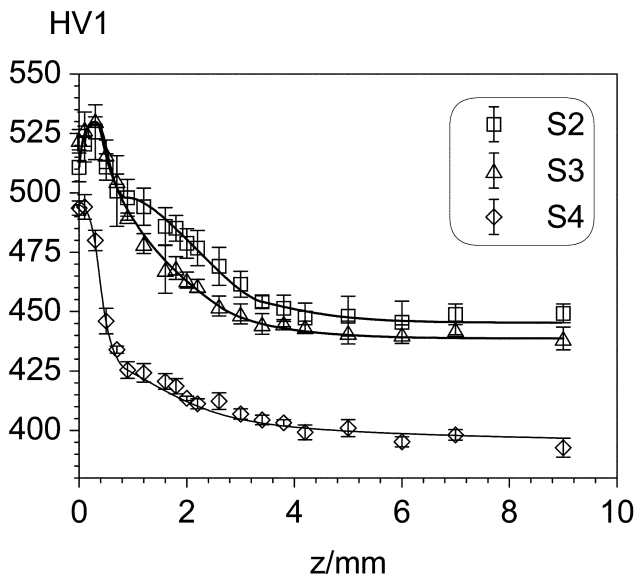

(*b*)

Fig. 1—Vickers hardness profiles of (*a*) the as-welded (S1) and conventional PWHT (S2) RR1000 samples and (*b*) the PWHT samples (S2, S3, and S4) as a function of axial distance from the weld line ($z = 0$) measured at the midwall thickness.

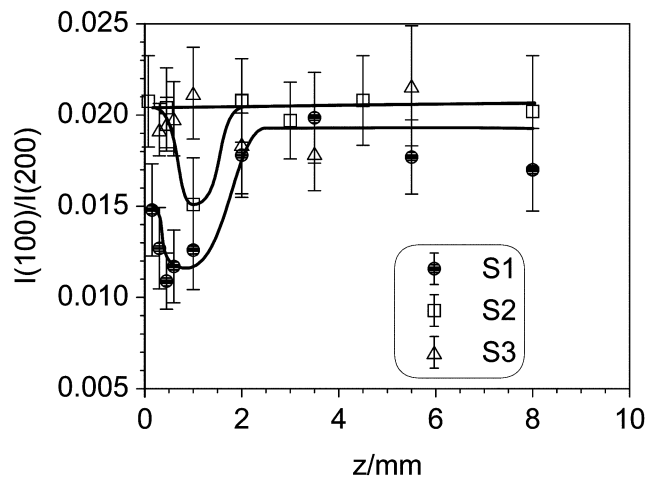

Fig. 2—The normalized (I(100)/I(200)) integrated intensity of the γ' superlattice reflection measured on ID11 at the ESRF plotted against the axial distance from the weld line.

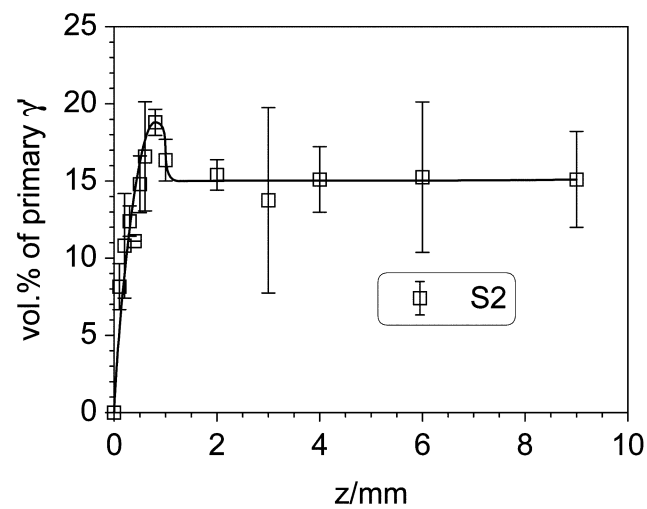

Fig. 3—Variation in primary γ' volume fraction with distance from the weld line as measured by quantitative metallography from FEGSEM images.

the microstructure across the weld line to gain a better understanding of the hardness profiles in the as-welded and PWHT conditions.

B. γ' *Distribution*

The (100) superlattice synchrotron X-ray reflection data in Figure 2 shows that the as-welded sample is depleted of γ' until at least 2 mm away from the weld line. It is notable that the hardness drop (Figure 1(a)) and the maximum depletion of γ' occur at approximately the same axial position. This suggests that a significantly lower content of γ' could be responsible for the hardness drop observed in Figure 1(a) for the as-welded sample. It is interesting to note that, between the weld line and 0.5 mm, the volume fraction of γ' appears to decrease, whereas the hardness profile increases. The reason for this is unclear at this stage.

The conventional heat-treated sample also shows a zone impoverished of γ' within 2 mm of the weld line, although the drop of the normalized integrated intensity is less pronounced than in S1. The drop in γ' could be responsible for the kink in the hardness curve (A in Figure 1(a)) at 1 mm. In common with the as-welded sample, the volume fraction of γ' decreases and the hardness increases between the weld line and 0.5 mm. Virtually no alteration in γ' volume fraction was observed for the modified PWHT sample S3 across the weld line, suggesting that this treatment is sufficient to homogenize the γ' volume fraction (though not necessarily its distribution between primary, secondary, and tertiary phases).

Figure 3 shows the variation in primary γ' volume fraction across the weld line for the conventional PWHT sample determined from low-magnification FEGSEM images. At the weld line, the volume fraction drops to zero, whereas

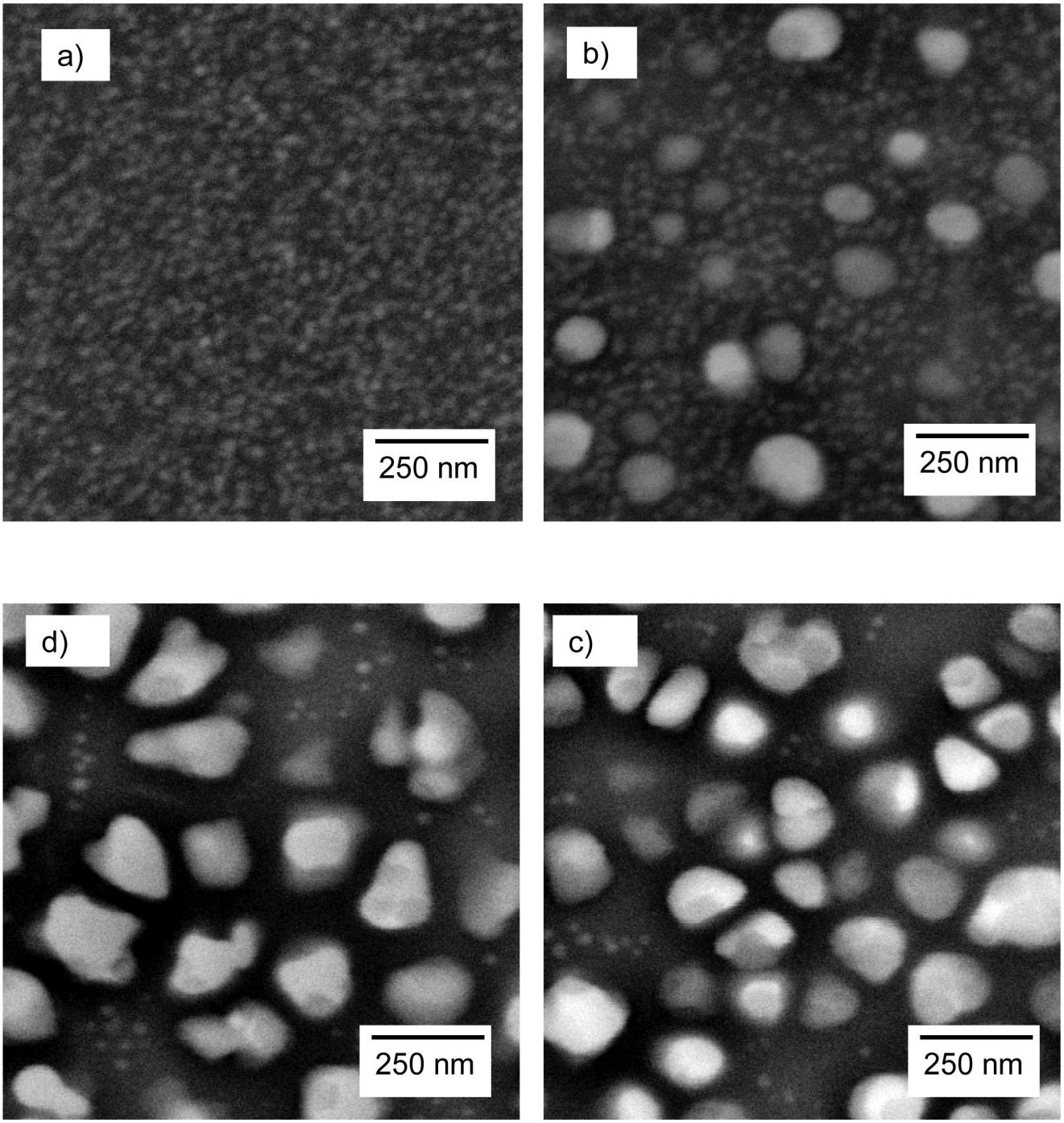

Fig. 4—Representative FEGSEM images of secondary and tertiary γ' of sample S3 (*a*) at the weld line, (*b*) 0.5 mm, (*c*) 2 mm, and (*d*) 9 mm from the weld line.

beyond 1 mm from the weld line the primary γ' content is essentially constant at approximately 15 pct. No significant change in primary γ' content was observed between the as-welded and PWHT samples. This was expected because primary γ' is stable in the range of heat-treatment temperatures used in this study.

Figures 4(a) through (d) are high-magnification FEGSEM images of sample S3 showing the distribution of secondary and tertiary γ' at various distances from the weld line. At the weld line, all secondary γ' is in solution, and only tertiary γ' was detected (Figure 4(a)). This feature was observed in the as-welded and all PWHT conditions. Significant changes in the secondary and tertiary γ' distribution can be observed over the first 2 mm from the weld line (Figures 4(a) through (c)). Comparing Figures 4(c) and (d), it is apparent that no significant changes in γ' occur beyond 2 mm from the weld line. This result is supported by Figure 5, which displays the FWHM variation of the superlattice reflection for samples S1, S2, and S3. The interpretation of the FWHM results is not straightforward because it can be influenced by several factors. For example, a diffraction peak can be broadened by lattice defects, such as dislocations (caused by work

hardening, for example), or by very small particle/grain sizes. Nevertheless, the constancy of FWHM with position beyond 2 mm suggests that the mean particle size of the small tertiary and secondary γ' does not change significantly beyond this distance.

The variation in secondary and tertiary γ' content is plotted against the axial position in Figure 6. The distribution of secondary γ' across the weld line is very similar for all samples. Essentially, no secondary γ' is present within 0.3 mm of the weld line beyond which it rises to a constant value of about 25 pct after 2 mm. Therefore, the volume fraction of secondary γ' cannot be directly correlated with the hardness profiles. Conversely, the change in volume fraction of tertiary γ' correlates well with the hardness peak close to the weld line. A sharp increase close to the weld line was measured for samples S3 and S4 and has been estimated in the way described previously for the as-welded and conventional PWHT samples (S1 and S2). The particle sizes of tertiary γ' at the weld line ($z = 0$ mm), measured by analyzing carbon replicas of samples S1, S2, and S3 and FEGSEM images of sample S4, are listed in Table IV. It can be seen that, in the as-welded condition, tertiary γ' at the weld line has a mean particle size of only 8 nm. The coarsening of tertiary γ' is slight in sample S2 (13 nm) and S3 (17 nm), whereas, in sample S4, the tertiary γ' has coarsened significantly (75 nm) because of the high heat-treatment temperature. In Figure 7, the particle size of secondary γ' is plotted as a function of the axial position. No significant change in the particle size could be observed between samples S1, S2, and S3. At 0.3 mm, the secondary γ' has a mean particle size of about 80 nm and increases up to about 180 to 200 nm beyond 2 mm from the weld line. This is in very good agreement with Reference 20, in which the particle size for secondary γ' in RR1000 was measured as 225 nm. Note the small increase in particle size for S1, S2, and S3 between 2 and 4 mm. This indicates minor changes in γ' distribution between 2 and 4 mm, which might be too small to observe during synchrotron studies. The high heat-treatment temperature of sample S4 has caused a significant coarsening of secondary γ' over the whole range, resulting in a mean particle size of about 300 nm across the entire region. One could argue that the smaller particle size of secondary γ' close to the weld line contributes to a higher hardness in this area. However, the content of secondary γ' is low in this area (Figure 6) so that the effect of tertiary γ' can be assumed to be dominant. In summary, the measurements have shown that, provided the postweld heat treatment temperature is in the range of interest (S2 and S3), aging leads to preferential coarsening of tertiary γ' with the secondary γ' particle size being largely

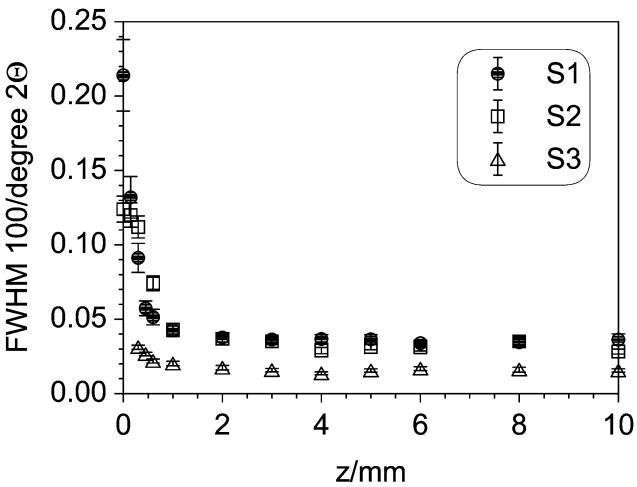

Fig. 5—FWHM (in degrees two theta) of the (100) X-ray superlattice reflection ($\theta = 1.62$ deg), recorded on ID11, plotted against the axial position for samples S1, S2, and S3.

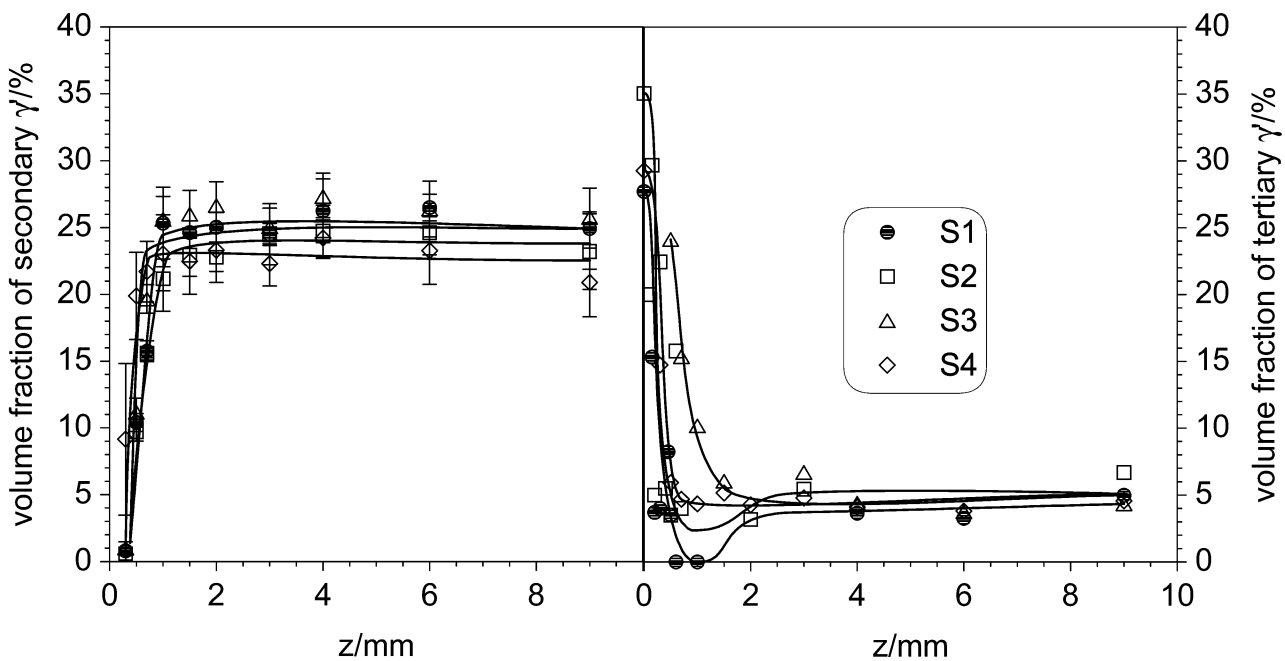

Fig. 6—Volume fraction of secondary (measured by image analysis) and tertiary γ' (calculated by subtracting the primary and secondary volume percent from the total γ' fraction determined from Fig. 2 for S1 and S2 and measured by image analysis for S3 and S4) against the axial position.

Table IV. Particle Size of Tertiary γ' Measured by Means of TEM and FEGSEM

	As-Welded (S1)	Conventional PWHT (S2)	Modified PWHT (S3)	Modified (2) PWHT (S4)
Method	TEM	TEM	TEM	SEM
Particle size/nm	8	13	17	75

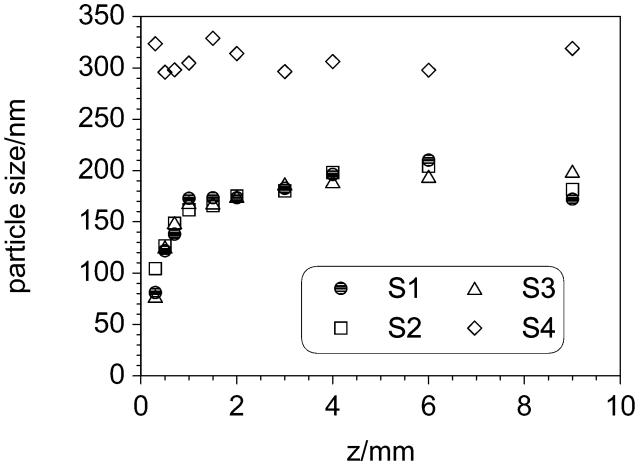

Fig. 7—Particle size of secondary γ' against the axial position measured from FEGSEM images.

unaffected. This observation has also been reported for UDIMET 720LI.[7]

Precipitation strengthening has been found to give three types of behavior as a function of γ' particle size.[21] At small precipitate radii (r), weakly coupled dislocations cut the precipitates, and the critical resolved shear stress (CRSS) increases as $r^{1/2}$. When r is slightly larger, the dislocations become strongly coupled (superdislocations), and the CRSS decreases. Finally, at large particle sizes, a gradual transition is observed to Orowan looping. For NIMONIC* 105 containing 51 pct γ', the change from weak to strong dislocation coupling occurred at 85 nm and from cutting to looping at 270 nm. Because alloys, such as NIMONIC 105, have a bimodal distribution of intragranular γ', cutting and bowing could be observed in the same sample.[22] For UDIMET 720LI,[7] the largest CRSS was calculated to correspond to a particle size of 40 nm, taking into account the models of weakly and strongly coupled dislocations but not Orowan bowing. From the measurements in this article, it can be concluded that it is the *tertiary* γ' that has a significant impact on the hardness profile. The importance of tertiary γ' in respect of mechanical properties has also been reported by Torster *et al.*,[23] where it was observed that an increased volume fraction of tertiary γ' resulted in a higher proof stress. In general, it is well accepted that an increase of the cooling rate from the solution temperature increases the tertiary γ' volume fraction and, thus, tensile strength.[24]

*NIMONIC is a trademark of INCO Alloys International, Inc., Huntington, WV.

In contrast to UDIMET 720LI,[7] the current hardness results suggest that the strongest particle size in the HAZ of RR1000 is significantly smaller than 40 nm because an increase of the mean tertiary γ' size from 13 to 17 nm (S2 to S3) at the weld line does not result in a significantly higher hardness. It is important to note that the strongest particle size is dependent on the volume fraction of γ' (a lower volume fraction of γ' implying a smaller strongest particle size), which according to Figure 2 also changes during postweld heat treatment. It is not clear how much of a decrease in hardness is caused by the small particle size (8 nm) of tertiary γ' in the HAZ of the as-welded condition. But, it is clear that the strongest particle size should be smaller in the HAZ of the as-welded condition compared to the PWHT condition because the overall volume fraction of γ' is lower in S1. The hardness profile shifts downwards when the tertiary γ' is significantly coarsened (S4). In summary, it is important to note that the γ' distribution can explain the hardness peak close to the weld line ($z = 0.3$ mm) but not the slight drop in hardness at the weld line and the gradual decrease of hardness between 2 and 4 mm from the weld line.

C. *HAGB Distribution*

Representative HAGB maps for sample S1 are shown in Figures 8(a) through (e). Because of the similar chemical composition and structure of γ and γ', the maps can not distinguish between γ grains and primary γ' particles. The maps show a dramatic change in microstructure between the weld line and 1 mm from the weld line. Beyond 1 mm from the weld line, no discernable change in microstructure was observed. At the weld line (Figure 8(a)), the high temperature reached has resulted in a fully recrystallized microstructure with a mean grain size of 3.7 μm and an even grain-size (D) distribution. The sharp drop of D between the weld line and 0.25 mm is partly due to the fact that, at the weld line, D is only determined by γ, whereas, at 0.25 mm, the mean grain size is a combination of γ and γ'. At 0.5 mm away from the weld line (Figure 8(c)), the microstructure exhibits large areas with very small grains where the microstructure has started to recrystallize under a combination of heavy plastic deformation and high temperature. Also large grains are visible, which have not yet started to recrystallize. The variation in grain size is presented as $D^{-0.5}$ across the weld line in Figure 9. In a small region, around 0.5 mm away from the weld line, the grain size is reduced by almost 50 pct. Jones[25] has estimated the relative effectiveness of the grain-boundary strengthening component from experimental work on NIMONIC PE16 and NIMONIC 105.[21,26] For NIMONIC 105, which contains ≈50 vol pct γ', the grain-boundary strengthening at 100-μm grain size was calculated to be about 70 MPa, resulting in a Hall–Petch coefficient, k, of 700 MPa $\mu m^{0.5}$. Applying this k coefficient to RR1000 (Figure 9) can only give a rough estimate of the strengthening effect of the grain boundaries but indicates an increase in strength at 0.5 mm of more than 150 MPa. Correlating Figure 9 with Figure 1(a) would suggest that the grain size does have an impact on the hardness peak very close to the weld line. It is noteworthy that, in the parent material (greater

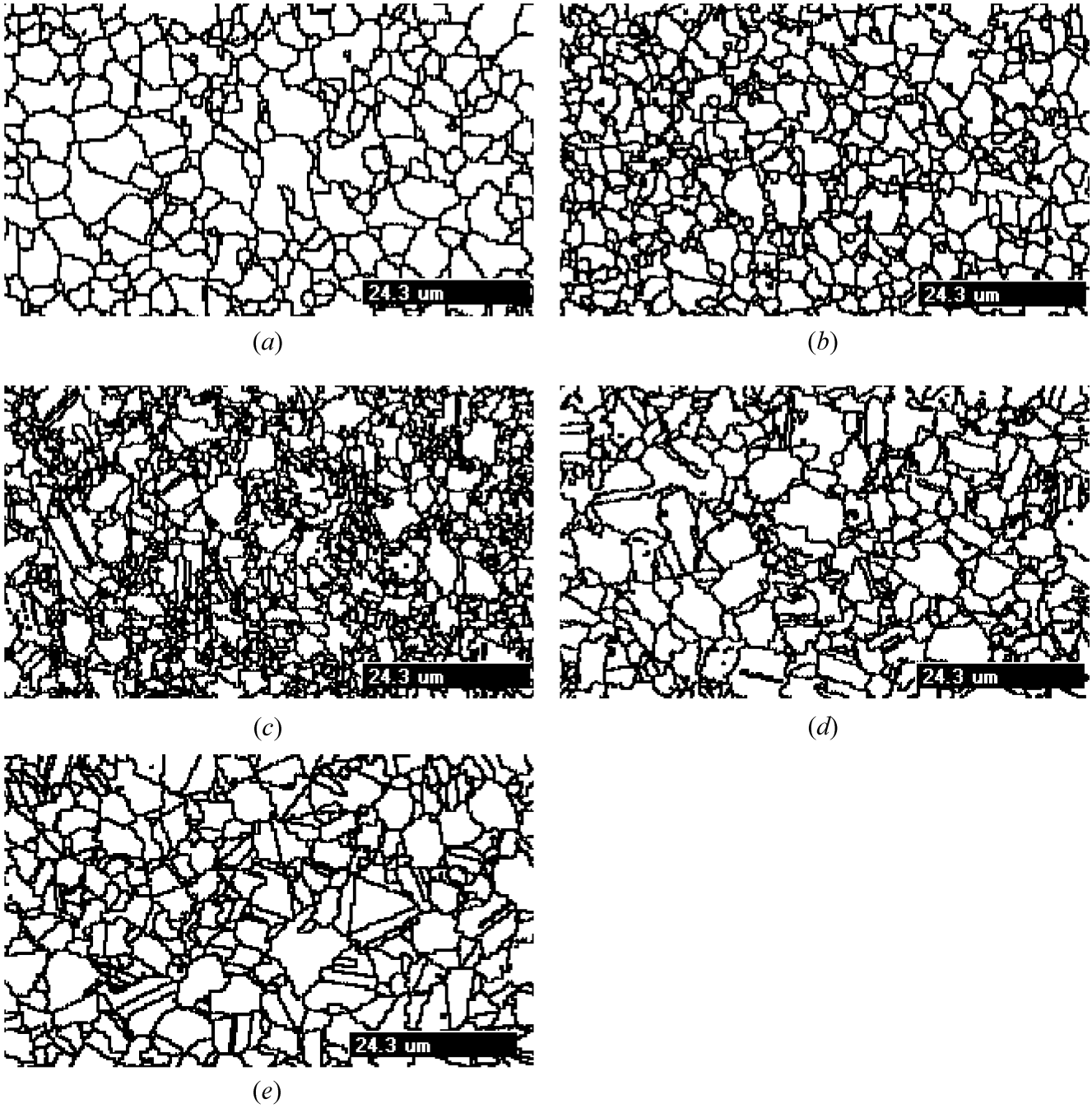

Fig. 8—EBSD maps showing high-angle grain boundaries for sample S1 (*a*) at the weld line and (*b*) 0.25 mm, (*c*) 0.5 mm, (*d*) 1 mm, and (*e*) 5 mm away from it. These are representatives of larger maps containing >1500 grains for which the average grain sizes are 3.66, 2.05, 1.43, 2.10, and 2.69 μm, respectively, and the percent twin boundaries 3.5, 5, 11, 18, and 27.

than 5 mm from the weld line), 27 pct of the HAGB were identified as twin boundaries, whereas, at the weld line, 3.5 pct of the HAGB are twins. This is a consequence of recrystallization at the weld line.

D. *Microtexture*

The EBSD mapping also allows a determination of the local texture. Negligible preferred orientation was recorded for all the (111) and (200) pole figures. The maximum intensity levels across the weld line do not exceed 2.25 × times random, indicating that texture does not play an important role with respect to mechanical properties.

E. *Work Hardening/γ/γ' Misfit*

One way to assess the change in the degree of work hardening is to measure the variation in diffraction-peak line broadening across the weld line. The interpretation of line broadening in terms of dislocation density and other factors is an established characterization technique.[27] However, in nickel superalloys, the interpretation of line width is more

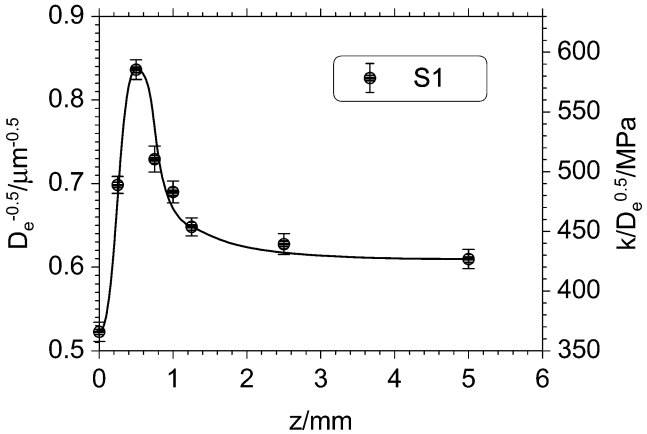

Fig. 9—The grain size in form of $D^{-0.5}$ across the weld line for sample S1 (as-welded) as recorded by EBSD mapping and the inferred Hall–Petch strengthening contribution (right hand abscissa).

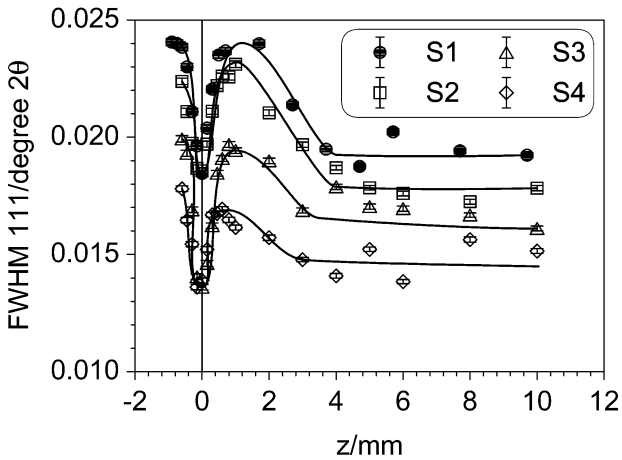

Fig. 10—FWHM of the (111) reflection as a function of the axial position recorded on ID11.

complicated than for single-phase materials because each main reflection consists of a γ and a γ' peak, which can not be resolved. Therefore, γ/γ' peak splitting also contributes to line broadening along with microstrain, plastic straining, and element partitioning between the two phases. Note, that this is in contrast to the behavior of the (100) reflection, which only results from changes in the γ' phase. In Figure 10, the FWHM is plotted in respect of the axial position for S1, S2, S3, and S4. It shows a gradual decrease of the FWHM between 2 and 4 mm that is most pronounced for the as-welded sample and becoming less pronounced as the postweld heat treatment temperature increases. This tendency is also reflected in the hardness profiles of the as-welded and PWHT samples. To clarify the possible impact of work-hardening changes on the FWHM within 4 mm of the weld line, an estimate of the stored energy of the as-welded sample (S1) was made for comparison from the EBSD maps. As with the FWHM, the stored energy rises sharply from the weld line to 0.5 mm (Figure 11). This is because of the recrystallized microstructure at the weld line, which contributes to the slight drop of hardness in this area. As can be seen in Figure 11, including the HAGBs in the stored energy does not significantly change the shape of

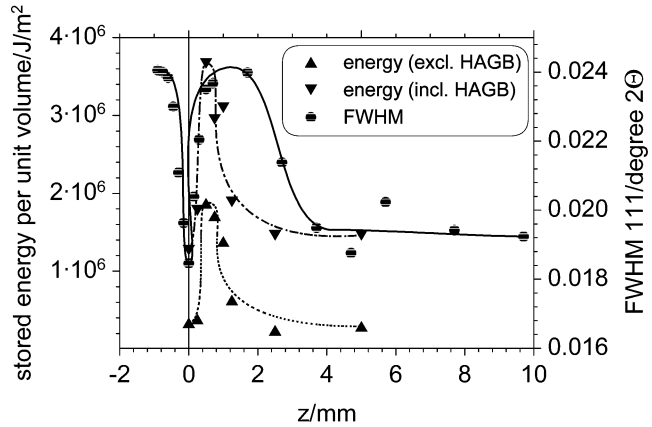

Fig. 11—Comparison of the stored EBSD and FWHM of (111) (synchrotron X-ray) across the weld line in sample S1 (as-welded).

the profile, only its magnitude. Although both measurement methods show peak values at around 0.5 mm, the calculated stored energy falls to the parent material value much nearer to the weld line (2 to 3 mm) than the FWHM measurement (4 mm). Therefore, it is probable that work hardening is only significant in the region leading up to the recrystallised zone (0.5 to 2 mm). As shown in Figure 4 in part II,[5] the mean lattice spacing of the (100) superlattice reflection (γ') changes dramatically within 4 mm from the weld line, whereas the mean (200) $\gamma + \gamma'$ lattice spacing shows only very moderate changes in the opposite direction. Because the observed (200) reflection comprises both a γ (200) and a γ' (200) reflection, the overall moderate shift of the (200) reflection in comparison to the (100) reflection can only be explained by a splitting of the γ and γ' reflections, which can be also seen in the peak broadening of the (111) reflection in Figure 10. This indicates an increase in misfit between the coherent γ and γ' within 4 mm from the weld line, resulting in a possible increase of strength.

IV. CONCLUSIONS

In this article, the microstructure of as-welded and variously PWHT RR1000 samples has been studied in detail. Hardness profiles have been recorded to map the variation of strength across the weld line. Subsequently, the microstructure has been studied by means of high-energy synchrotron X-rays, electron microscopy, and EBSD. The schematic shown in Figure 12 summarizes the effect of the main microstructural features on the hardness profiles for the as-welded (S1) and conventional PWHT (S2) samples. No single microstructural parameter determines the complete response. Instead, the variations in tertiary γ', work hardening, and grain-boundary strengthening are the most important microstructural features determining the hardness profiles across the joint line.

The as-welded sample (S1) begins to exhibit a significant increase in hardness around 4 mm from the weld line (Figure 1(a)). This change coincides only with increasing FWHM values and dramatic changes in the position of the (100) reflection.[5] These results indicate a splitting of the γ and γ' reflection because of an increase in misfit between those two phases, which might explain the early increase of hardness. The trough in hardness at 1 mm can be rationalized

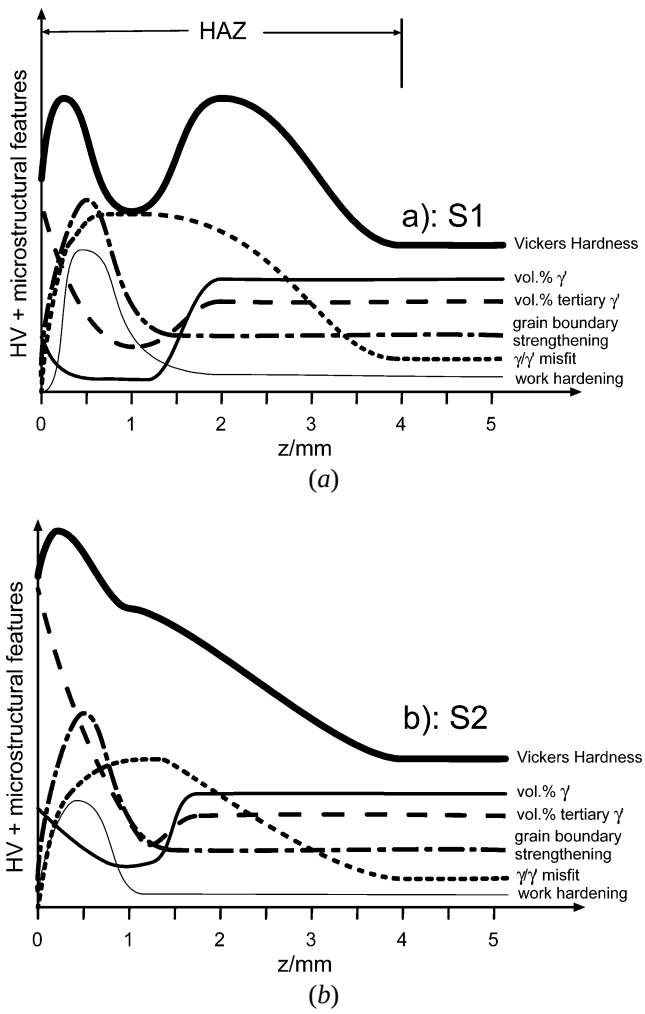

Fig. 12—Schematic illustrating the variation of the individual microstructural strengthening terms with distance from the weld line and the Vickers hardness for (*a*) the as-welded sample (S1) and (*b*) the conventional PWHT sample (S2). Note, volume fractions of γ' and tertiary γ' are not relative to each other.

by a depletion of tertiary γ' in this region (Figure 6). Within 2 mm from the weld line, the temperature history during inertia welding is sufficient to change the γ' distribution (HAZ), starting with the dissolution of tertiary γ', which could explain the hardness trough. On the other hand, the hardness peak near the weld line (around 0.5 mm) would seem to be explained by the small grain size arising from the beginning of recrystallization and a maximum in the stored energy. The fully recrystallized microstructure at the weld line, which results in a larger grain size and a lower degree of work hardening than in the region of the hardness peak, explains the slight hardness drop near the weld line itself. Because the size and volume fraction of γ' controls the optimum strengthening, it is difficult to say the location of the maximum γ' strengthening component. However, it does appear that the particle size of 8 nm at the weld line is smaller than the optimum in agreement with Reference 7 and that the optimum size is probably around 20 nm, which corresponds to that at the weld line after the postweld heat treatment.

The conventional PWHT (S2) shows a single hardness peak at 0.3 mm from the weld line (Figures 1(a) and (b)), which is 50 HV higher than in the as-welded condition. The variation of the γ' content around 1 mm from the weld line is less pronounced in sample S2 but still detectable, which could explain the slight kink of the hardness profile in this region. However, the larger volume fraction and particle size of tertiary γ' near the weld line compared to S1 appears to explain the increase of strength in the HAZ during postweld heat treatment.

As the postweld heat treatment temperature increases, the slope of the hardness profiles between 2 and 4 mm from the weld line (Figure 1(b)) is less steep. A postweld heat treatment temperature increase of 50 °C for the PWHT (S3) does not change the hardness profile significantly, whereas an increase of 150 °C (S4) clearly shifts the whole hardness profile downwards. Studies of secondary and tertiary γ' have shown that a moderate postweld heat treatment only slightly coarsens the tertiary γ'. When RR1000 is PWHT at a much higher temperature, both secondary and tertiary γ' coarsen significantly, which explains the low overall hardness for sample S4. These microstructural and hardness changes brought about by postweld heat treatment must be considered when relieving welding residual stresses to acceptable levels.[5]

ACKNOWLEDGMENTS

The authors thank Drs. A. Terry and G. Vaughan (ESRF, ID11), I. Brough and P.B. Kenway (MMSC) for experimental assistance, A. Thompson (Rolls-Royce) for producing the carbon replicas and analyzing TEM images, and J. Worsley (MMSC) for measuring two hardness profiles and analyzing FEGSEM images. These experiments are performed under the EPSRC Project No. GR/M68704 and are financially supported by EPSRC and Rolls-Royce plc.

REFERENCES

1. *Superalloys, Supercomposites and Superceramics*, J.K. Tien and T. Caulfield, eds., Academic Press Inc. (London) Ltd., London, 1989, pp. 142-43.
2. *The Superalloys*, C.T. Sims and W.C. Hagel, eds., John Wiley, New York, NY, 1972, pp. 509-32.
3. R. Spinat and Y. Honnorat: in *High Temperature Alloys for Gas Turbines and Other Applications*, W. Betz *et al.*, eds., Dordrecht D. Reidel, Butterworth-Heinemann, Ltd., Oxford, 1986, pp. 151-57.
4. M. Soucail, A. Moal, L. Nazé, E. Massoni, C. Leviallant, and Y. Bienvenu: in *Superalloys 1992*, S.D. Antolovich, R.W. Stusrud, R.A. Mackay, D.L. Anton, T. Khan, R.D. Kissinger, and D.L. Klarstrom, eds., TMS, 1992, pp. 847-56.
5. M. Preuss, J.W.L. Pang, P.J. Withers, and G. Baxter: *Mater. Trans A*, 2002, vol. 33A, pp. 3227-34.
6. S.J. Hessell *et al.*: U.S. Patent No. 5,897,718, Apr. 27, 1999.
7. M.P. Jackson and R.C. Reed: *Mater. Sci. Eng. A*, 1999, vol. 259, pp. 85-97.
8. P. Adam: *Welding of High Strength Gas Turbine Alloys*, Applied Science Publisher Ltd., London, 1978, pp. 737-68.
9. K.G. Schmitt-Thomas, P. Adam, H. Meisel, and R. Siede: *Z. Mettalkd.*, 1982, vol. 73 (9), pp. 558-65.
10. J.P. Ferte: *J. Phys. IV*, 1993, vol. 3, pp. 1019-27.
11. *Superalloys II, High Temperature Materials for Aerospace & Industrial Power*, C.T. Sims, N.S. Stoloff, and W.C. Hagel, eds., John Wiley & Sons Inc., New York, NY, 1987, pp. 221-26.
12. *The Superalloys*, C.T. Sims and W.C. Hagel, eds., John Wiley, New York, NY, 1972, p. 44.
13. A. Royer, P. Bastie, and M. Véron: *Scripta Mater.*, vol. 37, 1997, pp. 1199-1205.
14. A. Royer, P. Bastie, and M. Véron: *Scripta Mater.*, vol. 40, 1999, pp. 955-61.

15. A. Royer, P. Bastie, and M. Véron: *Acta Mater.*, 1998, vol. 46, pp. 5357-68.
16. Software and user manual at: http://www.umist.ac.uk/material/research/aluminum/frame.html.
17. W.T. Read: *Dislocations in Crystals*, McGraw-Hill, New York, NY, 1953.
18. L.E. Murr: *Interfacial Phenomena in Metals and Alloys*, Addison-Wesley, Reading, MA, 1975, p. 131.
19. Channel 4.2: HKL Technology ApS, Blaakildevej 17k, Hobro, DK-9500, Denmark.
20. A.J. Manning: Ph.D. Thesis, University of Cambridge, Cambridge, United Kingdom, 1999, p. 114.
21. B. Reppich, P. Schepp, and G. Wehner: *Acta Metall.*, 1982, vol. 30, pp. 95-104.
22. V. Seetharaman, K.B.S. Rao, D. Sundararaman, and P. Rodriguez: *Acta Metall.*, 1987, vol. 35, pp. 565-75.
23. F. Torster, G. Baumeister, J. Albrecht, G. Luetjering, D. Helm, and M.A. Daeubler: *Mater. Sci. Eng. A*, 1997, vol. A234, pp. 189-92.
24. J.J. Schirra and S.H. Goetschius: *Superalloys 1992*, S.D. Antolovich, R.W. Stusrud, R.A. Mackay, D.L. Anton, T. Khan, R.D. Kissinger, and D.L. Klarstrom, eds., TMS, Warrendale, PA, 1992, pp. 437-46.
25. J. Jones: Ph.D. Thesis, University of Cambridge, Cambridge, United Kingdom, 1997, p. 52.
26. W. Mangen and E. Nembach: *Acta Metall.*, 1989, vol. 37, pp. 1451-63.
27. B.D. Cullity: *Elements of X-ray Diffraction*, 2nd ed., Addison-Wesley Publishing Company, Reading, MA, 1978, pp. 284-92.